The Astrophysical Journal, 720:666–678, 2010 September 1 doi:10.1088/0004-637X/720/1/666
© 2010. The American Astronomical Society. All rights reserved. Printed in the U.S.A.

# DISENTANGLING THE CIRCUMNUCLEAR ENVIRONS OF CENTAURUS A. II. ON THE NATURE OF THE BROAD ABSORPTION LINE

D. Espada[1,2,3], A. B. Peck[4,5,6], S. Matsushita[1,4], K. Sakamoto[1], C. Henkel[7], D. Iono[8], F. P. Israel[9], S. Muller[10], G. Petitpas[5], Y. Pihlström[11,6], G. B. Taylor[11,6], and D. V. Trung[12,1]

[1] Academia Sinica, Institute of Astronomy and Astrophysics, P.O. Box 23-141, Taipei 10617, Taiwan
[2] Harvard-Smithsonian Center for Astrophysics, 60 Garden Street, Cambridge, MA 02138, USA; despada@cfa.harvard.edu
[3] Instituto de Astrofísica de Andalucía-CSIC, Apdo. 3004, 18080 Granada, Spain
[4] Joint ALMA Office, Av. El Golf 40, Piso 18, Las Condes, Santiago, Chile
[5] Harvard-Smithsonian Center for Astrophysics, Submillimeter Array, 645 North A'ohoku Place, Hilo, HI 96720, USA
[6] National Radio Astronomy Observatory, P.O. Box O, Socorro, NM 87801, USA
[7] Max-Planck-Institut für Radioastronomie, Auf dem Hügel 69, 53121 Bonn, Germany
[8] Nobeyama Radio Observatory, NAOJ, Minamimaki, Minamisaku, Nagano, 384-1305, Japan
[9] Sterrewacht Leiden, Leiden University, Postbus 9513, 2300 RA Leiden, The Netherlands
[10] Onsala Space Observatory, SE-43992 Onsala, Sweden
[11] Department of Physics and Astronomy, MSC07 4220, University of New Mexico, Albuquerque, NM 87131, USA
[12] Center for Quantum Electronics, Institute of Physics, Vietnam Academy of Science and Technology, 10 DaoTan, ThuLe, BaDinh, Hanoi, Vietnam
*Received 2010 April 7; accepted 2010 July 2; published 2010 August 12*

## ABSTRACT

We report on atomic gas (H I) and molecular gas (as traced by CO(2–1)) redshifted absorption features toward the nuclear regions of the closest powerful radio galaxy, Centaurus A (NGC 5128). Our H I observations using the Very Long Baseline Array allow us to discern with unprecedented sub-parsec resolution H I absorption profiles toward different positions along the 21 cm continuum jet in the inner 0.″3 (or 5.4 pc). In addition, our CO(2–1) data obtained with the Submillimeter Array probe the bulk of the absorbing molecular gas with little contamination by emission, which was not possible with previous CO single-dish observations. We shed light on the physical properties of the gas in the line of sight with these data, emphasizing the still open debate about the nature of the gas that produces the broad absorption line ($\sim$55 km s$^{-1}$). First, the broad H I line is more prominent toward the central and brightest 21 cm continuum component than toward a region along the jet at a distance $\sim$20 mas (or 0.4 pc) further from the nucleus. This indicates that the broad absorption line arises from gas located close to the nucleus, rather than from diffuse and more distant gas. Second, the different velocity components detected in the CO(2–1) absorption spectrum match well with other molecular lines, such as those of HCO$^+$(1–0), except the broad absorption line that is detected in HCO$^+$(1–0) (and most likely related to that of the H I). Dissociation of molecular hydrogen due to the active galactic nucleus seems to be efficient at distances $r \lesssim 10$ pc, which might contribute to the depth of the broad H I and molecular lines.

*Key words:* galaxies: elliptical and lenticular, cD – galaxies: individual (NGC 5128) – galaxies: ISM – galaxies: structure – quasars: absorption lines

*Online-only material:* color figures

## 1. INTRODUCTION

The analysis of absorption lines arising from atomic and molecular gas in galaxies is a powerful technique for studying the physical and chemical properties of the interstellar medium (ISM). Only a handful of nearby galaxies are known to show atomic (H I) and molecular absorption features. H I and molecular absorption line studies are not only relevant in deducing the properties of the ISM along specific lines of sight in nearby galaxies (e.g., Gupta et al. 2007) but are also essential for an interpretation of similar data toward higher redshift galaxies (e.g., Muller et al. 2006; Combes 2008; Henkel et al. 2009). Studying both H I and molecular gas absorption lines at the same time can reveal the interface between both components of the ISM at the circumnuclear regions where dissociation of molecular gas is expected as a result of energetic processes triggered by active galactic nuclei (AGNs).

At a distance of $D \simeq 3.8$ Mpc[13] (Harris et al. 2009), Centaurus A (Cen A, NGC 5128) is the nearest giant elliptical exhibiting nuclear activity, with powerful radio jets extending almost 10° on the sky and with prominent atomic and molecular emission as well as absorption features detected toward its nuclear regions (Israel 1998). It is thus a unique source to study the molecular to atomic interface. At this distance, high spatial resolution can be achieved: 1″ corresponds to 18 pc projected linear size. For a comprehensive general review of Cen A, see Israel (1998).

One of the most prominent features in Cen A is the dust lane along its minor axis, which is composed of a large amount of gas and dust within a warped disk-like structure seen nearly edge-on. An H I mass of $(10 \pm 3) \times 10^8\ M_\odot$ extends out to a radius of at least $r = 7'$ (or about 7 kpc), while it is observed to be mostly absent within the inner arcmin (or 1 kpc projected linear size; van Gorkom et al. 1990; Schiminovich et al. 1994; Israel 1998). A comparable amount of molecular gas is contained within the inner $r \simeq 2'$ (2 kpc), $M_{\rm H_2} \simeq 4.2 \times 10^8\ M_\odot$ (Eckart et al. 1990b). About 30%–40% of the total molecular gas content is located within the inner 1′ (1 kpc), $M_{\rm H_2} = (8.1 \pm 0.4) \times 10^7\ M_\odot$ (Espada et al. 2009, hereafter Paper I). A circumnuclear disk of molecular gas is resolved in the inner kiloparsec, with a size of $24'' \times 12''$ ($430 \times 215$ pc) in diameter, and with different kinematics with respect to the molecular gas at larger radii (Paper I).

Along the NE–SW direction (perpendicular to the circumnuclear molecular gas disk), there exists a spectacular radio-

[13] This distance is used throughout this paper.

continuum jet extending from the nucleus (parsec scale) to the outer radio lobes (hundreds of kilo-parsec scale). Subparsec-scale Very Large Baseline Interferometry (VLBI, including the VSOP-VLBI space observatory program), high resolution radio-continuum observations (e.g., at 2.3, 4.8, 8.4, 22.2, and 43 GHz) show that the structure of Cen A is rather complex, consisting of a bright nuclear jet and a fainter counterjet, as well as a bright central component (e.g., Tingay et al. 1998; Tingay & Murphy 2001; Horiuchi et al. 2006). Note that this component is not the nucleus itself since the nucleus is not bright at frequencies below 10–20 GHz due to synchrotron self-absorption and free–free absorption from a disk or torus of ionized gas (Jones et al. 1996; Tingay & Murphy 2001). The compact core becomes visible at mm/submm wavelengths (Kellermann et al. 1997) where its spectral index is quite flat (see Figure 6 in Meisenheimer et al. 2007).

H I absorption lines in this source were found for the first time four decades ago (e.g., Roberts 1970). Since then, Very Large Array (VLA) aperture synthesis observations with resolutions of the order of $\sim 10''$ (van der Hulst et al. 1983; Sarma et al. 2002) have shown H I absorption lines in different regions along the jet. They are distributed toward both the core and the inner jet (extended along $30''$) and are composed of a set of lines with widths of typically 10 km s$^{-1}$. The most prominent H I absorption component is located close to the systemic velocity of the galaxy ($V_{\rm LSR} = 541.6 \pm 2$ km s$^{-1}$; Israel 1998).[14] Toward the compact bright continuum component, two redshifted lines are seen at $V = 578$ km s$^{-1}$ and 598 km s$^{-1}$, as well as a broad absorption component (extending up to $V = 620$ km s$^{-1}$ with a width of $\Delta V \simeq 55$ km s$^{-1}$). Sarma et al. (2002) showed that the latter is only present toward the central component, but not along the other regions of the jet. This sets an upper limit on the size of the absorbing material of about $20''$, or 360 pc, as seen in projection.

Molecular absorption lines from centimeter to sub-millimeter wavelengths have also been detected for several species. At centimeter wavelengths, narrow molecular lines (a few km s$^{-1}$ width) close to the systemic velocity have been observed in several molecules such as OH, $H_2CO$, $C_3H_2$, and $NH_3$ (Gardner & Whiteoak 1976a, 1976b; Seaquist & Bell 1990; van Langevelde et al. 1995, 2005). Single-dish observations have been performed at millimeter/sub-millimeter wavelengths for the lowest transitions of CO, HCN, HNC, $HCO^+$, $H^{13}CO^+$, $N_2H^+$, $C_2H$, CN, and CS (Eckart et al. 1990a; Israel et al. 1990; Wiklind & Combes 1997; Eckart et al. 1999). In addition to narrow lines close to the systemic velocity, both narrow and broad absorption features are seen at redshifted velocities in $HCO^+$(1–0), OH 18 cm, and to a minor extent in HCN(1–0), HNC(1–0), and CS(2–1), covering a velocity range from $\sim$570 to 620 km s$^{-1}$ (e.g., Seaquist & Bell 1990; Eckart et al. 1990b; Israel et al. 1991; Wiklind & Combes 1997).

Although there is a consensus that narrow absorption lines with velocities close to the systemic velocity represent gas far from the nucleus, a dichotomy exists regarding the nature of the broad redshifted absorption line. It has been suggested that it might be: (1) warm and dense gas close to the nucleus and probably falling into it (e.g., van der Hulst et al. 1983; Israel et al. 1991), and (2) cold diffuse gas above and below a warped disk (Eckart et al. 1999). In this paper, we aim to shed light on the model that better represents the different gaseous components (both atomic and molecular) producing such absorption lines, and their physical properties as a result of their location with respect to the nucleus. In particular, we emphasize the origin of the broad line component.

We have carried out H I observations using the Very Large Baseline Array (VLBA) and the phased VLA[15] which allow us to derive the properties of the main H I absorption features seen toward the continuum source at 21 cm with unprecedented subparsec resolution (versus the $\sim$180 pc resolution in past VLA experiments). This is complemented by CO(2–1) observations (and isotopologues) at the Submillimeter Array (SMA;[16] Ho et al. 2004; Paper I) from which we can extract a CO(2–1) absorption profile with minimal contamination by emission. We introduce our VLBA H I and SMA CO(2–1) observations and the data reduction in Section 2, where we present the continuum maps and absorption spectra. In Section 3, we focus on the identification of the individual H I absorption components and the physical properties of their corresponding regions. We present our results on the CO(2–1) and $^{13}$CO(2–1) absorption lines in Section 4 and compare the H I absorption lines with those of molecular lines in Section 5. We discuss the results in Section 6 and summarize our findings in Section 7.

## 2. OBSERVATIONS AND DATA REDUCTION

The array configuration, phase center, primary and synthesized beam, achieved noise, and spectral resolution of our VLBA H I and SMA CO(2–1) observations are shown in Table 1. In the following, we explain in more detail our observational strategies and data reduction.

### 2.1. VLBA H I Observations

The VLBA H I observations were carried out on 1994 November 26. Due to its low declination (decl. $\simeq -43^\circ$), Cen A was observable for 2 hr with 8 of the 10 VLBA antennas and the phased VLA. The observations were made using two intermediate frequencies (IFs) of 2 MHz each. The IFs were centered on the redshifted H I line ($\nu_{\rm rest} = 1420.405752$ MHz, at a velocity of $V_{\rm LSR} = 541.6$ km s$^{-1}$). Global fringe fitting was performed using AIPS[17] task FRING with a solution interval of 6 minutes. Amplitude calibration was derived using the antenna gain and system temperature recorded at each antenna. Bandpass calibration was done using the calibrator 3C273 (J1229+0203). The continuum was obtained from line-free channels. Continuum subtraction was done in `Difmap` (Shepherd et al. 1995) using a model of `CLEAN` components made from several line-free channels. Subsequent editing and imaging of all data were also done using `Difmap`, using natural weighting. The resulting half-power beamwidth (HPBW) is $36.3 \times 7.2$ mas ($0.65 \times 0.13$ pc). The velocity resolution in these observations is 3.3 km s$^{-1}$, and the total velocity coverage of a single IF is $\sim$430 km s$^{-1}$.

### 2.2. SMA CO(2–1) Observations

Details of the CO(2–1) observations using the SMA in its compact configuration are reported in Paper I. CO(2–1), $^{13}$CO(2–1), and C$^{18}$O(2–1) lines were simultaneously observed. We used two independent sources, 3C273 and Callisto, to check the consistency of our bandpass calibration. Both solutions

[14] All velocities in this paper are radio LSR. Conversion from LSR to heliocentric velocity is $V_{\rm Hel} = V_{\rm LSR} + 2.4$ km s$^{-1}$.

[15] The VLBA and VLA are operated by the National Radio Astronomy Observatory, a facility of the National Science Foundation operated under cooperative agreement by Associated Universities, Inc.

[16] The Submillimeter Array is a joint project between the Smithsonian Astrophysical Observatory and the Academia Sinica Institute of Astronomy and Astrophysics and is funded by the Smithsonian Institution and the Academia Sinica.

[17] http://www.aips.nrao.edu/cook.html

**Table 1**
Main Parameters of the VLBA H I and SMA CO(2–1) Observations

| | |
|---|---|
| **H I VLBA Observations** | |
| Date | 1994 Nov 26 |
| R.A. of phase center (J2000) | $13^h25^m27.^s609$ |
| Decl. of phase center (J2000) | $-43^\circ01'07.''97$ |
| Time on source (hr) | 2 |
| FWHM of synthesized beam | 36.3 × 7.2 mas (0.65 × 0.13 pc), P.A. = 14.°8 |
| LSR velocity at band center (km s$^{-1}$) | 541.6 |
| Total bandwidth | 2 MHz (∼430 km s$^{-1}$) |
| Spectral resolution (km s$^{-1}$) | 3.3 |
| rms noise (3.3 km s$^{-1}$) | 3 mJy beam$^{-1}$ |
| rms (continuum map) | 2 mJy beam$^{-1}$ |
| **CO(2–1) SMA Observations** | |
| Date | 2006 Apr 5 |
| R.A. of phase center (J2000) | $13^h25^m27.^s6$ |
| Decl. of phase center (J2000) | $-43^\circ01'09''$ |
| On source time (hr) | 3 |
| FWHM of synthesized beam | 2.″4 × 6.″0 (43 × 108 pc), P.A. = 0.°82 |
| LSR velocity at band center (km s$^{-1}$) | 550 |
| Total bandwidth | 2 GHz (∼2870 km s$^{-1}$) in each sideband (separated by 10 GHz) |
| Spectral resolution (km s$^{-1}$) | 1 |
| rms noise (1 km s$^{-1}$) | 0.1 Jy beam$^{-1}$ (0.3 Jy beam$^{-1}$ for baselines >50 m) |

were nearly identical in most of the spectral windows, and in particular where the CO(2–1) lines were located. The continuum toward Cen A at 1.3 mm was found to consist of an unresolved source with a flux of $S_{1.3\,\mathrm{mm}} = 5.9 \pm 1.0$ Jy beam$^{-1}$ at the AGN position which was used to calibrate the data of Cen A itself (Paper I). No continuum subtraction was performed. The velocity resolution is 1 km s$^{-1}$.

In order to minimize undesired emission, we obtain the CO(2–1) absorption spectrum by directly fitting the amplitude of the interferometric visibilities using a point source model fixed at the position of the unresolved continuum source. This was done with the task `UV_FIT` in the `GILDAS`[18] reduction package. The CO(2–1) spectrum extracted using visibilities from all baselines still shows some emission at velocities $V$ = 420–510 km s$^{-1}$ and $V$ = 620–680 km s$^{-1}$. This corresponds to extended emission from the circumnuclear regions (Paper I). A new fit to the visibility data with projected baseline lengths ⩾50 m yielded a flatter spectral baseline. This is due to a combination of the spatial filtering capabilities of the interferometer, beam smearing and probably a lack of CO(2–1) emission toward the central ∼5″ (∼90 pc). The typical extent that we take into account by removing the shorter baselines can be roughly estimated as $\leqslant \lambda/D \simeq 4''$ (∼ 72 pc), where λ is the wavelength of the observations and $D$ the average baseline length.

We show in Figure 1 the resulting CO(2–1) spectra with and without visibilities with baseline lengths larger than 50 m. For the $^{13}$CO(2–1) and C$^{18}$O(2–1) transitions, however, we retained all visibilities since there is no significant emission down to our noise level. Their resulting noise per channel, $\sigma$ = 0.1 Jy, is thus smaller than in the long baseline only CO(2–1) spectrum ($\sigma$ = 0.3 Jy).

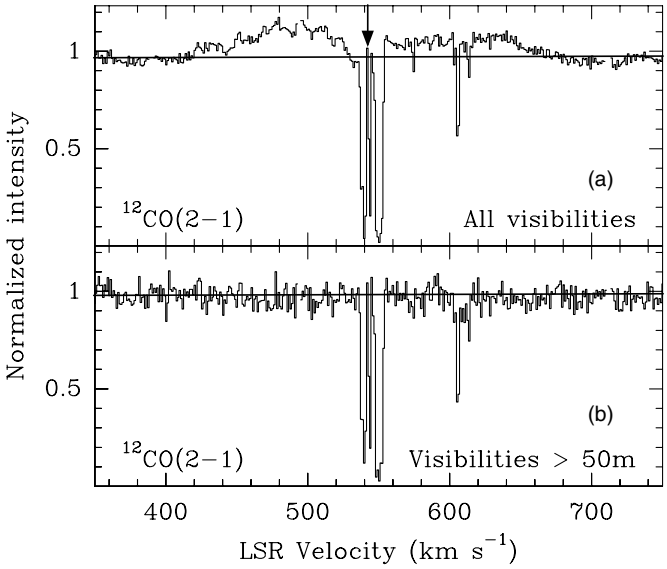


**Figure 1.** (a) CO(2–1) normalized intensity spectra obtained from all the visibilities using a fit in the UV plane assuming a point-like feature for the continuum emission. It clearly fails to eliminate most of the emission arising from the circumnuclear molecular gas (Espada et al. 2009). The arrow indicates the systemic velocity of the galaxy ($V$ = 541.6 km s$^{-1}$). (b) Same as (a) but only using visibilities with projected baselines larger than 50 m. The contamination by emission is efficiently diminished.

## 3. H I ABSORPTION FEATURES

### *3.1. 21 cm Continuum: Nuclear Jet*

The 21 cm continuum map in the inner 0.″3 (5.4 pc) is presented in Figure 2 (center). This high-resolution map resolves the bright 21 cm central component (∼10″ or 180 pc) found by van der Hulst et al. (1983) and Sarma et al. (2002; labeled as "Nucleus"). We find that this central component further comprises a more compact bright component and a nuclear jet extending up to 0.″23 to the NE, with a similar P.A. ≃ 51° as the inner 21 cm jet extending up to 55″ (van der Hulst et al. 1983; Sarma et al. 2002). Note that van Langevelde et al. (2005) present a VLBI 18 cm continuum map with a sub-arcsecond resolution where the central bright component is seen. However, the rest of the nuclear jet is not as clearly detected as in our map.

While the peak flux density is 603 mJy beam$^{-1}$ and the noise level of our maps is 2 mJy beam$^{-1}$, note that the uncertainty of

[18] http://www.iram.fr/IRAMFR/GILDAS

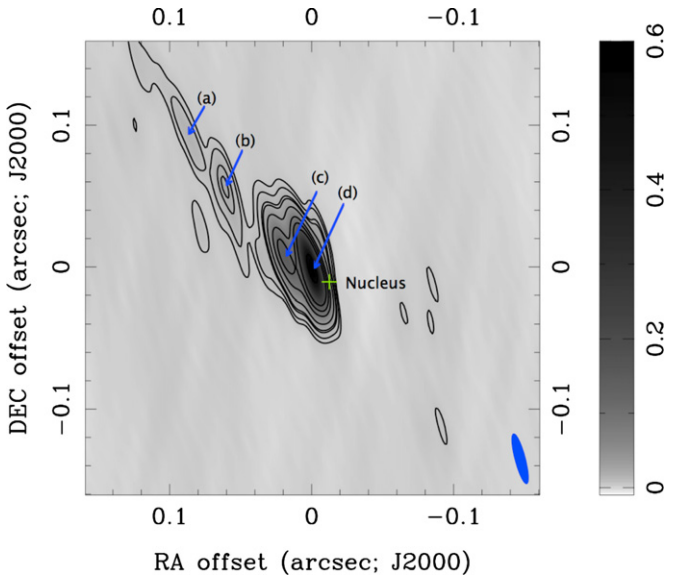


**Figure 2.** Nuclear jet of the 21 cm continuum emission of Cen A in the inner 0.″3 (or 5.4 pc), as observed with the VLBA. The brightest component has a flux density peak of $S_{21\mathrm{cm}} = 600 \pm 30$ mJy beam$^{-1}$. Note that this is not associated with the nucleus itself but with the base of the nuclear jet (Section 1). The cross indicates the approximate location of the 8.4 GHz continuum core (Tingay & Murphy 2001), assuming that the 1.4 GHz (or 21 cm) brightest component coincides with that of the 2.2 GHz emission. Contours are drawn at 3, 5, 9, 11, 20, 40, 60, 90, and 250 × $\sigma$, where $\sigma = 2$ mJy beam$^{-1}$. The gray scale ranges from −10 to 603 mJy beam$^{-1}$. The restoring beam is characterized by an HPBW = 36.3 × 7.2 mas and a position angle (P.A.) = 14.°8, as is shown by the filled ellipse in the lower right of the plot. Note that 1 mas corresponds to 0.018 pc.

(A color version of this figure is available in the online journal.)

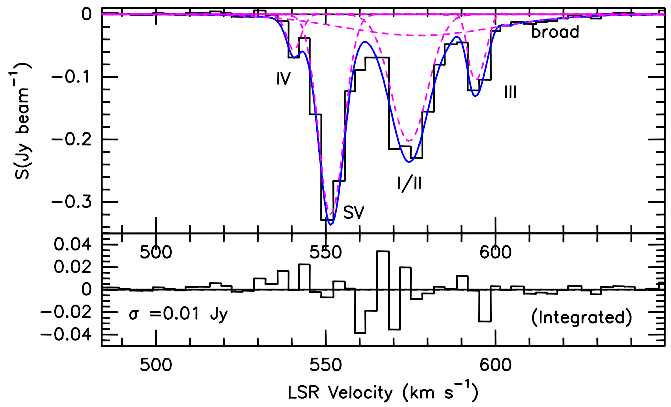


**Figure 3.** H I absorption profile of Cen A, integrated over the entire 21 cm continuum region probed by our VLBA experiment (Figure 2). The profile is mainly composed of five lines: IV, SV, I/II, and III, plus an underlying broader line with a width of 53 ± 10 km s$^{-1}$, whose wing is clearly seen at $V >$ 600 km s$^{-1}$. The velocity resolution is 3.3 km s$^{-1}$ and the rms noise of 3 mJy beam$^{-1}$ per channel. The solid line is the sum of the Gaussian fits to the individual lines (dashed lines, as specified in Table 2). The plot at the bottom shows the residual from this fit, with an rms $\sigma = 0.01$ Jy.

(A color version of this figure is available in the online journal.)

the absolute flux density measurement is larger. Uncertainties in flux calibration are estimated to be about 5% ($S_{21\mathrm{cm}} = 600 \pm 30$ mJy beam$^{-1}$). In addition, on-source errors due to deconvolution are expected. For instance, Tingay & Murphy (2001) estimated that the corresponding flux density error in their 2.2 GHz VLBA data of Cen A due to this effect is about 30% for the brightest components. This source of error is expected to be larger for our lower observing frequency, since the $uv$ coverage is less uniform.

As mentioned in Section 1, the core of the radio source has a very strongly inverted spectrum since the continuum emission is seen through a circumnuclear ionized gas disk which is opaque at wavelengths longer than 13 cm (or frequencies lower than 2.3 GHz) due to free–free absorption and to self-absorbed synchrotron emission (Jones et al. 1996; Tingay & Murphy 2001). The compact bright component in Figure 2 is thus part of the approaching jet and is offset from the actual AGN. Tingay & Murphy (2001) showed that there is an absolute offset of 12.5 mas to the east and 10.5 mas to the north between the 8.4 GHz and 2.2 GHz central components. This corresponds to a separation of 0.3 pc along the jet axis. We show in Figure 2 the estimated location of the AGN (8.4 GHz central component), assuming that the bright component of our 1.4 GHz map coincides with that of the 2.2 GHz map, and also that position variability between the different observing dates is not significant. We do not detect any continuum emission from the counterjet toward the SW to the 2 mJy beam$^{-1}$ noise level of our VLBA maps.

### 3.2. Identification of H I Absorption Features

Figure 3 shows the H I spectrum integrated over the entire continuum source. We find five main H I absorption lines: four relatively narrow lines and an underlying broad line. These absorption lines, all redshifted with respect to the systemic velocity, were detected using the VLA by van der Hulst et al. (1983) and Sarma et al. (2002), although toward an unresolved component of size ∼8″–10″. We adopt the nomenclature used in Sarma et al. (2002) for the most prominent lines (in roman numerals, IV, SV, I, II, and III).

We derive from Gaussian fits the mean velocities ($V$), peak flux densities ($S$), and full widths at half Maximum (FWHM) of the different lines in our H I profile, as shown in Table 2. We first fit the broad line using the redshifted wing at $V >$ 600 km s$^{-1}$, and then fit the remaining lines individually. An exception is line I/II, which is a blend of lines I and II in the H I spectra of Sarma et al. (2002). Being almost unresolved with our 3.3 km s$^{-1}$ resolution, we decided to compute them together.

**Table 2**
Parameters of H I Absorption Lines Integrated over the Entire 21 cm Continuum

| Absorption Feature | $V$ (km s$^{-1}$) | Peak $S$[a] (mJy beam$^{-1}$) | FWHM[a] (km s$^{-1}$) | Peak $\tau$ | $\int \tau dV$ (km s$^{-1}$) | $N$(H I)/$T_s$ (cm$^{-2}$ K$^{-1}$) |
|---|---|---|---|---|---|---|
| IV | 541 ± 1 | −57 ± 19 | 5 ± 2 | 0.13 ± 0.03 | 0.7 ± 0.4 | $(1.2 \pm 0.7) \times 10^{18}$ |
| SV | 552 ± 1 | −323 ± 20 | 8.5 ± 1.2 | 0.74 ± 0.03 | 7.7 ± 1.0 | $(14 \pm 2) \times 10^{18}$ |
| I, II | 575 ± 1 | −203 ± 17 | 12.6 ± 1.6 | 0.48 ± 0.02 | 7.6 ± 0.9 | $(14 \pm 2) \times 10^{18}$ |
| III | 595 ± 1 | −122 ± 20 | 5.2 ± 1.4 | 0.25 ± 0.03 | 1.8 ± 0.4 | $(3.2 \pm 0.7) \times 10^{18}$ |
| Broad | 578 ± 4 | −34 ± 21 | 53 ± 10 | 0.07 ± 0.03 | 4.0 ± 1.9 | $(7 \pm 3) \times 10^{18}$ |

**Note.** [a] Flux density peak and FWHM are calculated from a Gaussian fit.

**Table 3**
Parameters of H I Absorption Lines Toward Individual Positions[a]

| Absorption Feature | $V$ (km s$^{-1}$) | Peak $S$ (mJy beam$^{-1}$) | FWHM (km s$^{-1}$) | Peak $\tau$ | $\int \tau dV$ (km s$^{-1}$) | $N$(H I)/$T_s$ (cm$^{-2}$ K$^{-1}$) |
|---|---|---|---|---|---|---|
| (a) | | | | | | |
| IV | (541) | <2 | (5) | <0.6 | <2 | $<4 \times 10^{18}$ |
| SV | 552 ± 1 | −2 ± 3 | 4 | <0.6 | <2 | $<4 \times 10^{18}$ |
| I/II | (575) | <2 | (14) | <0.6 | <3 | $<11 \times 10^{18}$ |
| III | (595) | <2 | (6) | <0.6 | <2 | $<5 \times 10^{18}$ |
| Broad | (578) | <2 | (50) | <0.6 | <6 | $<43 \times 10^{18}$ |
| (b) | | | | | | |
| IV | (541) | <17 | (5) | <0.3 | <1 | $<2 \times 10^{18}$ |
| SV | 552 ± 1 | 9 ± 2 | 5 ± 3 | 0.81 ± 0.07 | 4 ± 2 | $(7 \pm 3) \times 10^{18}$ |
| I/II | (575) | <17 | (14) | <0.3 | <2 | $<7 \times 10^{18}$ |
| III | (595) | <17 | (6) | <0.3 | <1 | $<4 \times 10^{18}$ |
| Broad | (578) | <17 | (50) | <0.3 | <4 | $<30 \times 10^{18}$ |
| (c) | | | | | | |
| IV | 541 ± 1 | 129 ± 5 | 5 ± 2 | 0.12 ± 0.02 | 0.7 ± 0.3 | $(1.3 \pm 0.5) \times 10^{18}$ |
| SV | 551 ± 1 | 59 ± 5 | 6.3 ± 1.0 | 0.90 ± 0.02 | 5.5 ± 1.0 | $(10 \pm 2) \times 10^{18}$ |
| I/II | 576 ± 1 | 108 ± 5 | 13 ± 2 | 0.29 ± 0.02 | 4.4 ± 0.7 | $(8.0 \pm 1.3) \times 10^{18}$ |
| III | 596 ± 1 | 120 ± 5 | 5 ± 2 | 0.18 ± 0.02 | 1.2 ± 0.4 | $(2.2 \pm 0.7) \times 10^{18}$ |
| Broad | 578 ± 4 | 142 ± 5 | 53 ± 10 | 0.01 ± 0.02 | 0.5 ± 1.1 | $(1 \pm 2) \times 10^{18}$ |
| (d) | | | | | | |
| IV | 540 ± 1 | 546 ± 10 | 3 ± 2 | 0.10 ± 0.03 | 0.5 ± 0.2 | $(0.9 \pm 0.4) \times 10^{18}$ |
| SV | 551 ± 1 | 286 ± 10 | 7.7 ± 1.3 | 0.75 ± 0.03 | 6.7 ± 1.1 | $(12 \pm 2) \times 10^{18}$ |
| I/II | 574 ± 1 | 400 ± 10 | 12.8 ± 1.8 | 0.41 ± 0.03 | 5.9 ± 0.9 | $(10.7 \pm 1.7) \times 10^{18}$ |
| III | 595 ± 1 | 506 ± 10 | 5.6 ± 1.6 | 0.18 ± 0.03 | 1.5 ± 0.4 | $(2.7 \pm 0.7) \times 10^{18}$ |
| Broad | 577 ± 4 | 564 ± 10 | 55 ± 10 | 0.06 ± 0.03 | 3.6 ± 1.3 | $(7 \pm 2) \times 10^{18}$ |

**Note.**
[a] Velocity ($V$), flux density peak (peak $S$), FWHM (full width half maximum), peak optical depth (peak $\tau$), and integrated optical depth ($\int \tau dV$) were derived from Gaussian fits. Velocities in parentheses are assumed values in the fitting. Uncertainties in the flux density peak and the peak optical depth correspond to the residuals after Gaussian fitting (see Figure 4). Uncertainties in the integrated optical depth are calculated as the uncertainty of the area of the Gaussian profile. Upper limits in the integrated optical depth are $3\sigma$ and are calculated as $3 \times \sigma \times (\Delta V\ \delta v)^{1/2}$, where $\Delta V$ is the velocity of the integrated profile and $\delta v$ is the channel spacing. Line SV in position $a$ is detected, but the optical depth cannot be calculated since the absorption depth is larger than the continuum level due to the noise. Thus, we consider it as an upper limit.

The H I absorption features in our spectra are located at $V = 541$, 552, 575, and 595 (±1) km s$^{-1}$ (IV, SV, I/II, and III, as outlined in Figure 3). The most prominent lines show FHWM values of about 5–10 km s$^{-1}$. A fit to the broad absorption line yields an FWHM = 53 ± 10 km s$^{-1}$ centered at 578 ± 4 km s$^{-1}$. The final fit and the resulting residual from the observed H I profile are presented in Figure 3.

The great advantage of our VLBA data is that we can obtain the H I absorption spectrum toward different positions over the continuum emission. Figure 2 shows the four most prominent continuum sources where we obtained H I absorption profiles. Their relative offsets with respect to the phase center are: $(\Delta\alpha, \Delta\delta) = (+73, +69)$ mas, $(+63, +58)$ mas, and $(+20, +10)$ mas (namely, positions $a$, $b$, and $c$), corresponding to separations of 1.8 pc, 1.5 pc, and 0.4 pc, respectively, as well as toward the brightest component at $(+1, -1)$ mas (namely, position $d$). The continuum flux density peaks of the different components are $S_{21cm} = 11$, 23, 145, and 603 mJy beam$^{-1}$, respectively.

While we detect H I absorption features only close to the systemic velocity (components IV and SV) in positions $a$ and $b$, in positions $c$ and $d$ the profiles show two additional redshifted H I absorption components I/II and III at $V =$ 574–576 km s$^{-1}$ and 595–596 km s$^{-1}$ (Figure 4). An additional shallow redshifted wing in position $d$ is clearly seen at velocities $V > 600$ km s$^{-1}$, which corresponds to the broad absorption line. The fitted Gaussian parameters are presented in Table 3, and the fits are shown in Figure 4. To fit these lines, we set as initial values the velocities and FWHM found for the H I absorption lines integrated over the entire continuum. Since the flux densities refer to their corresponding continuum emission, we calculated next the optical depths and H I column densities in order to compare between different positions.

### 3.3. H I Optical Depths and Column Densities

We calculated the H I optical depths, $\tau_{HI}$, as $I_{obs}[Jy] = I_{cont} e^{-\tau_{HI}}$, where $I_{obs}$ is the observed flux in absorption and $I_{cont}$ is the measured continuum flux. Absolute flux uncertainties do not have any effect on the optical depth since it is derived from the $I_{obs}/I_{cont}$ ratio. In Columns 5 and 6 of Tables 2 and 3, we present the H I optical depth peak (peak $\tau_{HI}$) and integrated optical depths ($\int \tau_{HI} dV$) integrated over the entire continuum source and for each independent position, respectively. The upper limits corresponding to non-detected lines are calculated as $3\sigma\ (\Delta V\ \delta v)^{1/2}$, where $\Delta V$ is the FWHM in Table 2 and $\delta v$ is the channel spacing of 3.3 km s$^{-1}$.

In Figure 5, we plot $\tau_{HI}$ toward the four different positions $a$, $b$, $c$, and $d$ along the 21 cm nuclear jet. The main absorption line is component SV, with peak $\tau_{HI} \geqslant 0.75$ seen at all positions. No trend is seen as a function of distance from the nucleus. On the other hand, the redshifted velocity component I/II seems to be preferentially deeper if closer to the brightest component (position $d$). Component I/II is characterized by peak $\tau_{HI} = 0.29 \pm 0.03$ in position $c$, while peak $\tau_{HI} = 0.41 \pm 0.02$ in position $d$. The $3\sigma$ upper limit obtained in position $b$ is peak

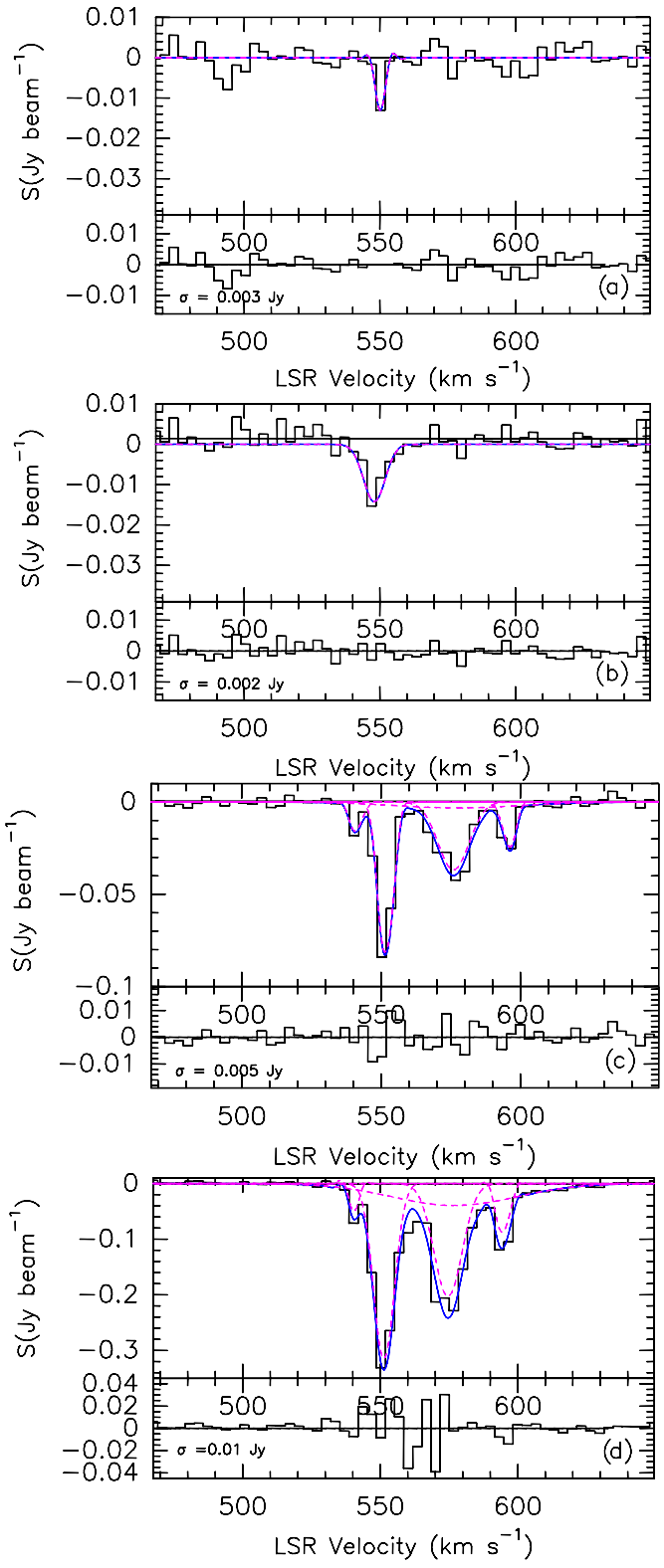


**Figure 4.** H I absorption lines toward single pixels at positions *a*, *b*, *c*, and *d* as outlined in Figure 2 (see bottom right of each panel), as well as the individual Gaussian fits and underlying final fitted curve. The residuals from the fit are characterized by a $\sigma$ as indicated on the lower left of each panel.

(A color version of this figure is available in the online journal.)

$\tau_{\rm H\,I} < 0.3$. However, we would have expected at least a tentative detection for component I/II in position *b* if of comparable depth as in position *c* or *d*.

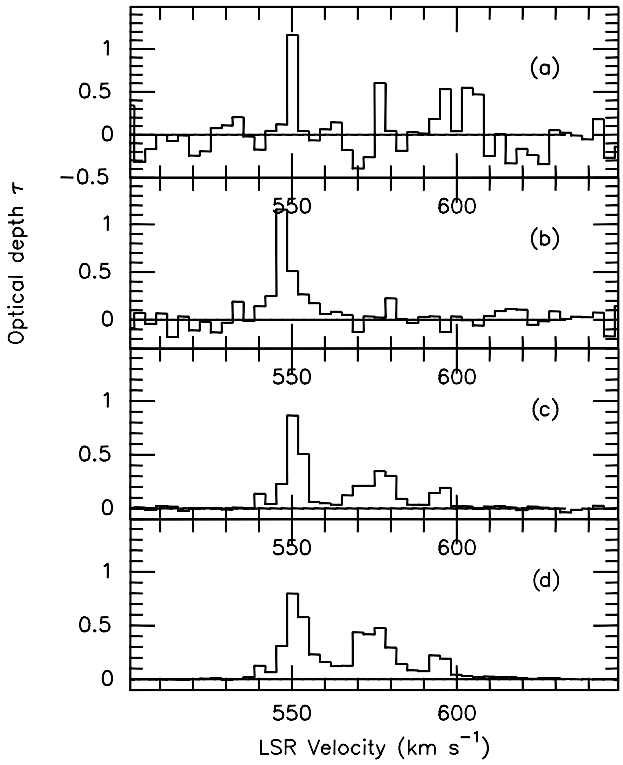


**Figure 5.** H I optical depths for the four different positions along the 21 cm jet (*a*, *b*, and *c*) and brightest component (*d*), as outlined in Figure 2. Positions are indicated at the upper right of each panel.

It is surprising that we detect the broad line component against the position *d* but it is weaker toward the adjacent continuum region, position *c*. Figure 6 shows a close-up of the $\tau_{\rm H\,I}$ in both locations. A fit to the broad component (assuming that a Gaussian function applies) gives integrated optical depths of $\int \tau_{\rm H\,I} dV = 3.6 \pm 1.3$ km s$^{-1}$ for position *d* while it is $\int \tau_{\rm H\,I} dV = 0.5 \pm 1.1$ km s$^{-1}$ in position *c* (Table 3). That the broad absorption line in position *c* is weaker is reinforced by the smaller optical depths in the spectral regions between the lines SV, I/II, and III at $V = 560$ km s$^{-1}$ and 590 km s$^{-1}$ with respect to position *d* (Figure 6). This implies that the H I opacity of the broad line component varies within a projected linear scale of less than 0.4 pc.

Finally, we calculate the H I column densities (Column 7 in Tables 2 and 3), using the following relation:

$$N({\rm H\,I})/T_{\rm s}[{\rm cm^{-2}\,K^{-1}}] = 1.823 \times 10^{18} \int \tau_{\rm H\,I} dV[{\rm km\,s^{-1}}],$$

where $T_{\rm s}$ is the spin temperature. The H I column densities in the different lines cover the range $N({\rm H\,I})/T_{\rm s} \sim (1\text{–}12) \times 10^{18}$ cm$^{-2}$ K$^{-1}$. The broad line toward position *d* has a corresponding $N({\rm H\,I})/T_{\rm s}$ that is comparable to the deepest narrow lines.

## 4. CO(2–1) ABSORPTION FEATURES

In our 1.3 mm observations, with a restoring beam of $6\farcs0 \times 2\farcs4$ (or 110 × 40 pc), we found an unresolved continuum source at the galactic center (Paper I). The inner jet observed at cm wavelengths has a steep radio spectrum so the contribution at mm wavelengths is negligible (Israel et al. 2008). Therefore, our 1.3 mm continuum emission is dominated by the nuclear continuum emission. The angular size of the central

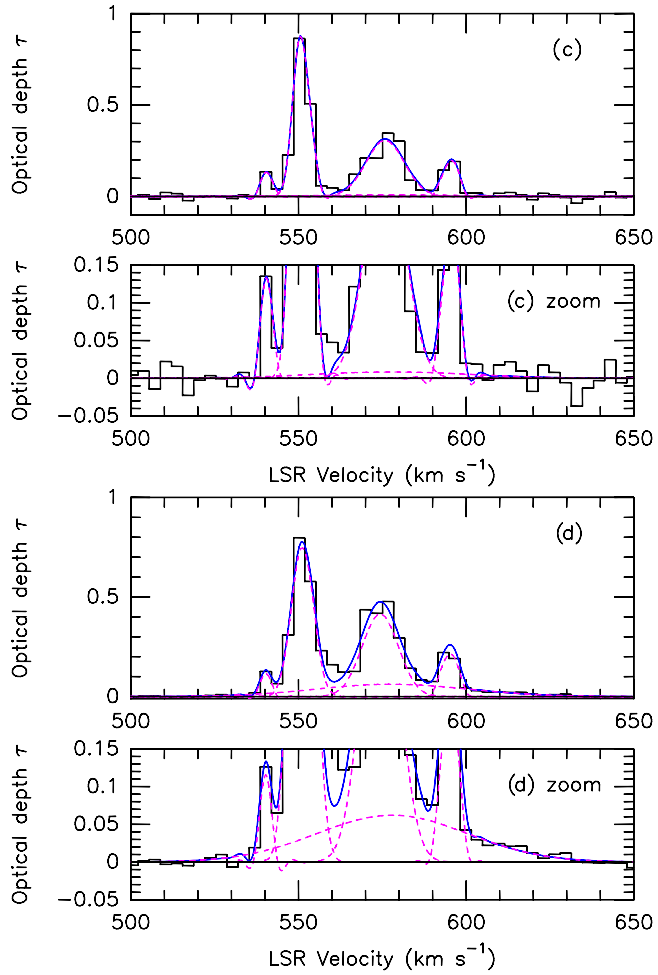


**Figure 6.** Fits to the H I optical depth ($\tau$) profiles at positions *c* (top) and *d* (bottom). A zoom in optical depth from −0.05 to 0.15 is included to emphasize the weak lines.

(A color version of this figure is available in the online journal.)

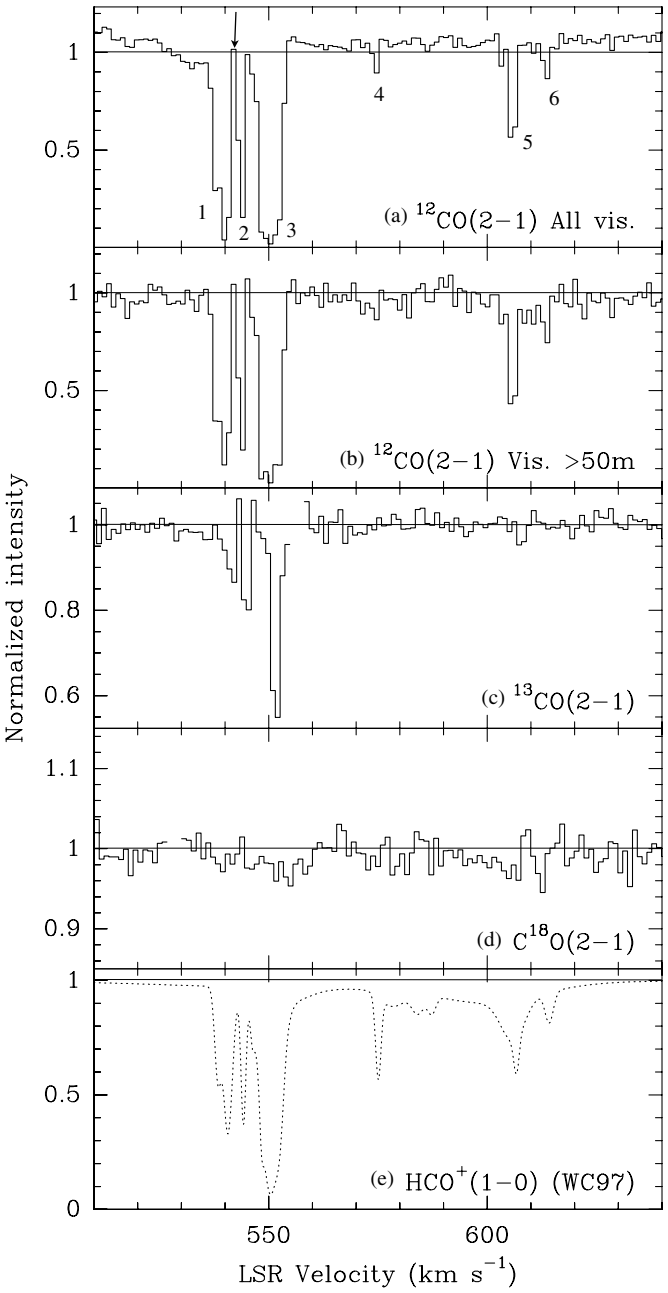


**Figure 7.** (a) CO(2–1) normalized intensity spectrum using all visibilities. Numbered labels indicate the different molecular gas absorption components. (b) CO(2–1) spectrum only with projected baselines longer than 50 m. (c) $^{13}$CO(2–1) spectrum. The three main features close to the systemic velocity are detected. (d) C$^{18}$O(2–1) spectrum. No absorption lines have been detected with our sensitivity. No emission is seen either in the $^{13}$CO(2–1) or the C$^{18}$O(2–1) spectra, therefore we include all the visibilities. (e) Gaussian fits to the single-dish HCO$^+$(1–0) spectrum (Wiklind & Combes 1997). The arrow indicates the systemic velocity ($V = 541.6$ km s$^{-1}$).

continuum source is 0.5 ± 0.1 mas at 43 GHz, or 0.009 ± 0.002 pc (Kellermann et al. 1997), and is considerably smaller than our synthesized beam. The absorption spectra of CO(2–1), $^{13}$CO(2–1), and C$^{18}$O(2–1) (the latter two taking into account all visibilities) are shown in Figures 7(b)–(d), respectively. Absorption features have been detected in CO(2–1) and $^{13}$CO(2–1), but not in C$^{18}$O(2–1) at a 3$\sigma$ level (= 0.3 Jy).

### *4.1. CO(2–1) Line Characterization*

The CO(2–1) absorption spectrum spans a range of 540 km s$^{-1}$ < $V$ < 620 km s$^{-1}$ and is composed of six narrow lines. The narrow absorption features are labeled as outlined in Figure 7(a): lines 1, 2, and 3 correspond to the absorption lines close to the systemic velocity, at $V = 539$, 544, and 550 km s$^{-1}$, and 4, 5, and 6 to absorption lines at higher velocities, located at $V$ = 575, 606, and 613 km s$^{-1}$ (Table 4). Component 4 is clearly detected in the profile with all visibilities, but it turns out to be weak with only the longest baselines due to the increase of noise level. CO(2–1) absorption line 2 is located in the most likely systemic velocity of the galaxy. Absorption lines 1, 2, and 3 are much deeper than the higher velocity components, with component 3 the most prominent.

Three $^{13}$CO(2–1) absorption lines are also detected, corresponding to features 1, 2, and 3 in the CO(2–1) profile. An additional line corresponding to CO(2–1) line 5 was tentatively detected. Features 4 and 6 are not detected at a 3$\sigma$ level.

The line widths are comparable in most cases to our spectral resolution. Because of the limited velocity resolution of our SMA observations (1 km s$^{-1}$) and the narrowness of the absorption lines, we do not attempt to fit Gaussian functions to several CO(2–1) line components. Line widths in the CO(2–1) profile of components 1 and 3 are about $\Delta V$ = 3–5 km s$^{-1}$, while the remaining lines have even smaller line widths $\Delta V \simeq$ 1–2 km s$^{-1}$. Lines with widths less than 1–2 km s$^{-1}$ are not

**Table 4**
Parameters of the CO(2–1), $^{13}$CO(2–1), and C$^{18}$O(2–1) Absorption Lines

| Isotope | Line | $V$ (km s$^{-1}$) | $S$ (Jy beam$^{-1}$) | Peak $\tau$ | $\int \tau dV$ (km s$^{-1}$) | $N$(CO)[a] ($10^{14}$ cm$^{-2}$) | $N$(H$_2$)[b] ($10^{18}$ cm$^{-2}$) |
|---|---|---|---|---|---|---|---|
| $^{12}$CO(2–1) | 1 | 539 | 0.72 ± 0.25 | 2.1 ± 0.3 | 6.00 ± 0.10 | 616 ± 10 | 725 ± 12 |
| | 2 | 544 | 1.20 ± 0.25 | 1.6 ± 0.2 | 2.33 ± 0.07 | 239 ± 7 | 281 ± 8 |
| | 3 | 550 | 0.16 ± 0.25 | $\geqslant$ 3.6 | $\geqslant$ 14.88 | $\geqslant$ 1530 | $\geqslant$ 1800 |
| | 4 | 575 | 5.33 ± 0.25 | 0.10 ± 0.05 | 0.22 ± 0.03 | 23 ± 3 | 26 ± 4 |
| | 5 | 606 | 2.66 ± 0.25 | 0.80 ± 0.10 | 1.68 ± 0.07 | 172 ± 7 | 203 ± 8 |
| | 6 | 613 | 4.61 ± 0.25 | 0.25 ± 0.06 | 0.48 ± 0.07 | 49 ± 7 | 58 ± 8 |
| $^{13}$CO(2–1) | 1 | 541 | 5.30 ± 0.10 | 0.11 ± 0.02 | 0.35 ± 0.03 | 36 ± 3 | 3600 ± 300 |
| | 2 | 545 | 4.90 ± 0.10 | 0.19 ± 0.02 | 0.46 ± 0.03 | 47 ± 3 | 4700 ± 300 |
| | 3 | 552 | 3.33 ± 0.10 | 0.58 ± 0.03 | 1.42 ± 0.04 | 145 ± 4 | 14500 ± 400 |
| | 4 | ... | ... | ... | < 0.08 | < 8 | < 800 |
| | 5 | 607 | 5.80 ± 0.10 | 0.05 ± 0.01 | 0.10 ± 0.02 | 10 ± 2 | 1000 ± 200 |
| | 6 | ... | ... | ... | < 0.09 | < 9 | < 900 |
| C$^{18}$O(2–1) | ... | ... | ... | ... | < 0.11 | <11 | < 6600 |

**Notes.**
[a] Isotopic CO column densities. We assume a filling factor of unity, local thermodynamic equilibrium (LTE) and an excitation temperature $T_{ex} = 10$ K for the absorbing molecular gas (Section 4.2). Note that the CO(2–1) line 3 is likely saturated, so the optical depth and the column densities are lower limits. $^{13}$CO lines 4 and 6 and C$^{18}$O lines are not detected, thus we use upper limits taken at a $3\sigma$ level.
[b] H$_2$ column density ($N$(H$_2$)) derived from the CO(2–1) absorption lines (and isotopes). To derive the $N$(H$_2$) from the CO(2–1) lines, we use an abundance ratio of [CO]/[H$_2$] = 8.5 × $10^{-5}$ (Frerking et al. 1982), [$^{13}$CO]/[H$_2$] = 1 × $10^{-6}$ (Solomon et al. 1979), and [C$^{18}$O]/[H$_2$] = 1.7 × $10^{-7}$ (Frerking et al. 1982) ([CO]/[$^{13}$CO] = 85 and [CO]/[C$^{18}$O] = 500]).

(or insufficiently) resolved. Note that in those cases the optical depths are underestimated.

### 4.2. CO(2–1) Optical Depths and Column Densities

Since the radio core is small (∼0.009 pc; Kellermann et al. 1997), the covering factor is likely close to unity. In fact, the components close to the systemic velocity (1, 2, and 3) have depths >0.8, and assuming that $f \geqslant$ depth of absorption for a normalized spectrum (continuum flux is unity), the covering factor is $f > 80\%$. For simplicity, we adopt a filling factor $f$ of unity for all the components.

We have calculated the CO(2–1) optical depths $\tau_{CO(2-1)}$ in the same manner, $I_{obs}[Jy] = I_{cont} e^{-\tau_{CO(2-1)}}$ (Table 4), as those of H I. The optical depths for any undetected $^{13}$CO(2–1) and C$^{18}$O(2–1) lines have been calculated using a $3\sigma$ level upper limit. CO(2–1) component 3 is saturated since the depth of the absorption line nearly equals the continuum level, and $\tau_{CO(2-1)}$ is highly uncertain due to nonlinearity of the logarithmic function. High values of peak $\tau_{CO(2-1)}$ show that components 1, 2, and 3 are optically thick. CO(2–1) components 4, 5, and 6, as well as all of the $^{13}$CO(2–1) lines, are characterized by peak $\tau_{CO(2-1)} \lesssim 0.8$. Thus, they can be considered as optically thin if the filling factor is unity.

Our CO(2–1) optical depths agree reasonably well with previous single-dish measurements. The peak $\tau_{CO(2-1)}$ for components 1, 2, and 3 are $\tau_{CO(2-1)} = 2.1 \pm 0.3$, $1.6 \pm 0.2$, and $\geqslant 3.6 \pm 1.6$, respectively, which are compatible with those obtained by Israel et al. (1991), $\tau_{CO(2-1)} = 1.8^{+0.8}_{-0.5}$, $1.9^{+0.8}_{-0.5}$, and $\geqslant 3$. Israel et al. (1991) also give an optical depth for component 4 of $\tau_{CO(2-1)} = 0.4 \pm 0.2$, while our value is $0.10 \pm 0.05$. The remaining lines were not detected by Israel et al. (1991). This comparison shows the need for interferometric observations in order to minimize confusion by emission and obtain higher accuracy.

As for the $^{13}$CO(2–1) lines, the peak $\tau_{^{13}CO(2-1)}$ values are: $0.11 \pm 0.02$, $0.19 \pm 0.02$, $0.58 \pm 0.03$, and $0.05 \pm 0.01$ for components 1, 2, 3, and 5. Eckart et al. (1990a) give a peak optical depth of 0.4 for the line close to $V = 550$ km s$^{-1}$ and non-detections for the rest of the lines. This value is well in agreement with our component 3.

We derive column densities of each CO(2–1), $^{13}$CO(2–1), and C$^{18}$O(2–1) lines using the following equation:

$$N(\mathrm{CO}) = \frac{8\pi\nu^3}{c^3 A_{ul} g_u} \frac{Q(kT_{ex}) \exp(E_J/kT_{ex})}{(1 - \exp(-h\nu/kT_{ex}))} \int \tau_{CO(2-1)} dV,$$

where we assume that LTE conditions apply. $E_J$ denotes the energy of the lower level of the transition, $T_{ex}$ denotes the excitation temperature, $Q(T_{ex}) = \sum_J (2J+1) \exp(-E_J/kT_{ex})$ denotes the partition function, and $A_{ul}$ denotes the Einstein coefficient of each isotopologue. We use $T_{ex} = 10$ K, although it could vary depending on the properties and location of the molecular clouds. Indeed, a gradient in the excitation temperature has been inferred using a nominal temperature ratio of CO(2–1) and CO(1–0) emission line ratios by Israel et al. (1990, 1991): $T_{ex} \simeq 10$ K at $r > 1'$ (>1 kpc) while it seems to be larger in the circumnuclear gas ($r < 20''$), $T_{ex} \simeq 25$ K.

The different detected lines show CO column densities $N$(CO) spanning 2 orders of magnitude (Table 4), from $(23 \pm 3) \times 10^{14}$ cm$^{-2}$ (component 4) to $\geqslant 1530 \times 10^{14}$ cm$^{-2}$ (component 3). $N$(CO) increases approximately an order of magnitude if a $T_{ex} = 100$ K is used. The $^{13}$CO column density is in the range $<8 \times 10^{14}$ cm$^{-2}$ (component 4) and $(145 \pm 4) \times 10^{14}$ cm$^{-2}$ (component 3).

We list in Table 4 the H$_2$ column densities ($N$(H$_2$)) assuming abundance ratios [CO]/[H$_2$] = 8.5 × $10^{-5}$ (Frerking et al. 1982), [$^{13}$CO]/[H$_2$] = 1 × $10^{-6}$ (Solomon et al. 1979), and [C$^{18}$O]/[H$_2$] = 1.7 × $10^{-7}$ (Frerking et al. 1982). The H$_2$ column densities as obtained from CO(2–1) should be similar to those obtained with $^{13}$CO(2–1). However, $N$(H$_2$) obtained with CO(2–1) are systematically smaller than those obtained using $^{13}$CO(2–1). The [CO]/[$^{13}$CO] ratios for the six lines in order of increasing velocity are: $17 \pm 2$, $5 \pm 1$, $\geqslant 10$, $> 3$, $17 \pm 7$, and >5. These abundance ratios are considerably smaller than the assumed [CO]/[$^{13}$CO] = 85, similar to the local value. This

deviation in the abundance ratios might be due to a combination of the following reasons: (1) different excitation temperatures for $^{12}$CO and $^{13}$CO, (2) optical depth effects, (3) different filling factors, and (4) chemistry, such as fractionation through charge exchange reactions. However, low abundance ratios of ∼25 have been observed toward the Galactic center and PKS 1830−211 (see Table 7 of Muller et al. 2006)

### 4.3. $[^{12}C]/[^{13}C]$ and $[^{16}O]/[^{18}O]$ Isotopic Ratios

We can roughly estimate the $[^{12}C]/[^{13}C]$ and $[^{16}O]/[^{18}O]$ isotopic ratios from the $[CO]/[^{13}CO]$ and $[^{13}CO]/[C^{18}O]$ ratios, assuming that the molecular abundance ratios can be decomposed into isotopic abundance ratios of the atoms. If we assume that $[^{12}CO]/[^{13}CO] = [^{12}C]/[^{13}C]$, then we obtain that $[^{12}C]/[^{13}C] \simeq 5$–17. The $[^{12}C]/[^{13}C]$ ratio is a measure of the primary to secondary processing: while $^{12}$C mostly arises from massive stars, $^{13}$C is predominantly produced from reprocessing of $^{12}$C from earlier stellar generations (e.g., Wilson & Rood 1994).

From our observations, we derive lower limits from the abundance ratio $[^{13}CO]/[C^{18}O]$. It ranges from >2 to >12. This is somewhat less restrictive than the $[^{13}CO]/[C^{18}O] > 30$ obtained by Wild et al. (1997) using the $J = 1$–0 absorption line, although their spectral resolution is a factor of 2 lower (∼1.9 km s$^{-1}$). Higher spectral resolution observations, with a channel width of 0.23 km s$^{-1}$, had been previously carried out by Israel et al. (1991). Israel et al. report a $2\sigma$ detection in the $C^{18}O$ line for component 3, which gives a value for the abundance ratio $[^{13}CO]/[C^{18}O] \simeq 13 \pm 3$. This would be in agreement with our lower limit, but not with that in Wild et al. (1997).

We can then obtain $[^{16}O]/[^{18}O]$ from our previous estimate of $[^{12}C]/[^{13}C]$. $^{16}$O and $^{18}$O form in massive stars and are predicted to behave similarly, except at early stages of massive star formation since $^{16}$O is a primary element and $^{18}$O is a secondary one (Prantzos et al. 1996). The ratio is therefore expected to decrease with time and stellar processing (e.g., Muller et al. 2006).

By adopting $[^{12}C]/[^{13}C] = 5$–17 and $[^{13}CO]/[C^{18}O] \simeq 13 \pm 3$ (Israel et al. 1991) (component 3), then $[^{16}O]/[^{18}O] \sim 70$–220. This ratio would be in agreement with values ∼150–200 in nearby starburst galaxies such as NGC 253 and NGC 4945 (Wang et al. 2004; Harrison et al. 1999; Henkel et al. 1993).

Overall, the $[^{12}C]/[^{13}C]$ and $[^{16}O]/[^{18}O]$ ratios in Cen A are closer to those found toward the Galactic center than to starburst galaxies (Henkel et al. 1993), and seems to indicate high metallicity and CNO burning by stars of intermediate mass over a long time interval.

On the other hand, note that Wiklind & Combes (1997) derived an isotopic ratio $[^{12}C]/[^{13}C] > 70$ for component 3 from its $[HCO^+]/[H^{13}CO^+]$ ratio, which yields $[^{16}O]/[^{18}O] >$ 200–840. This seems to contradict our results and shows the need of a systematic chemical study using different isotopic molecular lines.

## 5. COMPARISON OF ATOMIC AND MOLECULAR ABSORPTION LINES

In this section, we compare the variations of $\tau_{HCO^+(1-0)}/\tau_{CO(2-1)}$ and $\tau_{CO(2-1)}/\tau_{H\,I}$ in order to infer the variation of molecular to atomic abundances with velocity. As a zeroth-order approximation we consider three assumptions: (1) absorption lines of different species (both molecular and atomic) that have similar velocities are physically related, (2) temperature (and spin) differences vary similarly for different species so that the ratios are reasonably constant, and (3) molecular abundance ratios are reasonably constant ($[CO]/[H_2]$ and $[HCO^+]/[H_2]$).

### 5.1. Molecular Gas as Traced by CO(2–1) and $HCO^+$(1–0)

The different velocity components detected in the CO(2–1) absorption spectrum correspond well to other molecular lines, such as those of $HCO^+$(1–0). We chose $HCO^+$(1–0) for comparison because it traces molecular gas with different physical conditions (its critical density is 2 orders of magnitude larger than that traced by CO(2–1)). It is also the best signal-to-noise ratio and the highest spectral resolution (≃ 0.2 km s$^{-1}$) absorption profile that can be found in the literature (Wiklind & Combes 1997). The CO(2–1) absorption profile can be compared to that of $HCO^+$(1–0) (Figure 7(e)), which results from the sum of 17 Gaussian components used by Wiklind & Combes (1997) to parameterize the observed $HCO^+$(1–0) absorption spectrum. The more prominent lines of the $HCO^+$(1–0) spectrum are centered at the same velocities and have similar widths to their CO(2–1) counterparts. Note that no variability was found in different epochs for the $HCO^+$(1–0) absorption spectrum (Wiklind & Combes 1997), so we do not expect to find variability in our CO(2–1) profiles either.

On the other hand, the high velocity component (HVC) of the $HCO^+$(1–0) absorption profile (Wiklind & Combes 1997; Eckart et al. 1999; Figure 7(e)) is more prominent than in our CO(2–1) spectrum (Figure 7(b)). The broad component of $HCO^+$(1–0) absorbs roughly 15% of the continuum emission (Wiklind & Combes 1997). If the CO(2–1) broad absorption feature were as deep as the $HCO^+$(1–0) broad line then we would have detected it.

We derive the abundance ratio assuming $T_{ex} = 10$ K for CO(2–1) and $T_{ex} = 5$ K for $HCO^+$(1–0) (Wiklind & Combes 1997). For lines within 540 km s$^{-1}$ $V < 570$ km s$^{-1}$, the total abundances of $HCO^+$ and CO are $N(HCO^+) \simeq 4.8 \times 10^{13}$ cm$^{-2}$ (Table 8; Wiklind & Combes 1997) and $N(CO) \simeq 2.3 \times 10^{17}$ cm$^{-2}$, which provides the ratio $[HCO^+]/[CO] \simeq 2 \times 10^{-4}$. In the HVC, $V > 570$ km s$^{-1}$, the ratio is five times larger than in the low velocity components (LVCs), $[HCO^+]/[CO] \simeq 1 \times 10^{-3}$.

The $[HCO^+]/[CO]$ ratio is even larger within 570 km s$^{-1}$ $< V <$ 600 km s$^{-1}$. While $[HCO^+]/[CO] \simeq 5 \times 10^{-4}$ for components at $V > 600$ km s$^{-1}$, in the velocity range between 570 km s$^{-1}$ $< V <$ 600 km s$^{-1}$ it is a factor 10 larger, $[HCO^+]/[CO] \simeq 5 \times 10^{-3}$. This difference arises in the velocity range corresponding to the broad absorption component.

### 5.2. Atomic Versus Molecular Gas Content

In Figure 8, we present a comparison between the H I and CO(2–1) absorption features. It is important to note that we are tracing both the H I component *d* and molecular gas in the line of sight within a region located close by (≲0.3 pc).

A wide range of atomic to molecular abundance ratios are seen. While the main H I absorption features are located between $V = 544$ and 600 km s$^{-1}$, in CO and other molecules the main absorption features occur close to the systemic velocity, and then at larger velocities, $V > 605$ km s$^{-1}$. The H I absorption features are remarkably more prominent at 560 km s$^{-1}$ $< V <$ 610 km s$^{-1}$ than their molecular counterparts. The two components 5 and 6 of the CO(2–1) and $HCO^+$(1–0) spectra at $V > 605$ km s$^{-1}$ are located in the same velocity range as the H I broad absorption feature which is seen up to $V = 640$ km s$^{-1}$.

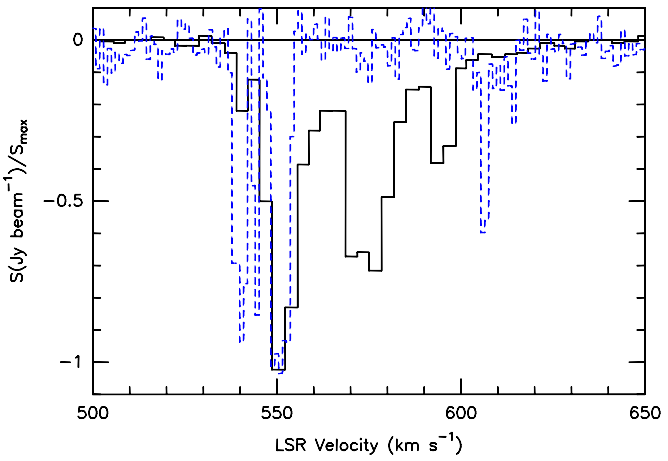


**Figure 8.** Comparison of the $^{12}$CO(2–1) (dashed line) and the H I absorption profiles (solid line). The velocity resolution is 1 km s$^{-1}$ and 3.3 km s$^{-1}$ for CO(2–1) and H I, respectively.

(A color version of this figure is available in the online journal.)

Next, we compare the molecular to atomic abundance ratio assuming $T_{ex} = 10$ K for CO(2–1) and $T_s = 100$ K for H I. First, in the LVC the gas is mostly in its molecular phase. The CO(2–1) line 1 seems to be related to the H I component IV, and it yields a ratio $N(H_2)/N(H\,I) = (7.25 \times 10^{20}\ cm^{-2})/(0.9 \times 10^{20}\ cm^{-2}) \simeq 8$. The $N(H_2)/N(H\,I)$ ratio corresponding to CO(2–1) line 2 is similar to that of the CO(2–1) line 1. The H I absorption line SV and CO(2–1) line 3, the ratio of $H_2$ to H I column densities is $N(H_2)/N(H\,I) \geqslant (1800 \times 10^{18}\ cm^{-2})/(12 \times 10^{20}\ cm^{-2}) = 1.5$.

In the HVC located between 570 km s$^{-1}$ < $V$ < 600 km s$^{-1}$, the gas is predominantly either atomic or molecular gas traced by HCO$^+$(1–0), but not by CO(2–1). H I lines I/II and III contain a total of $N(H\,I) \simeq (13.4 \pm 2) \times 10^{20}\ cm^{-2}$. If spatially linked to molecular clouds with the same kinematics, they would only correspond to CO(2–1) line 4, which contains a smaller amount of molecular gas, $N(H_2) \simeq (26 \pm 4) \times 10^{18}\ cm^{-2}$. The ratio is $N(H_2)/N(H\,I) \simeq 0.02$, 2–3 orders of magnitude smaller than in the LVCs. However, we have to add the contribution from the molecular gas column density traced by other coexisting species such as HCO$^+$(1–0) in this velocity range. Wiklind & Combes (1997) estimated it to be $N(HCO^+)/N(H\,I) \simeq 1.5 \times 10^{-8}$, or $N(H_2)/N(H\,I) \simeq 0.2$–2 assuming a typical $[HCO^+]/[H_2] = 10^{-7}$–$10^{-8}$. Even with the contribution of HCO$^+$ in the velocity range between 570 km s$^{-1}$ < $V$ < 600 km s$^{-1}$, we obtain a slightly smaller $[H_2]/[H\,I]$ ratio than in the LVC.

Finally, from $V$ > 600 km s$^{-1}$, CO(2–1) components 5 and 6 are within the H I broad line. There, $N(H\,I) = 7 \times 10^{20}\ cm^{-2}$ (broad line), to be compared to the $N(H_2) \simeq 2.6 \times 10^{20}\ cm^{-2}$, which yields a ratio $N(H_2)/N(H\,I) \simeq 0.4$.

## 6. DISCUSSION

### 6.1. Warped Disk or Non-circular/Infalling Motions?

Although there is a consensus that narrow absorption lines with velocities close to the systemic velocity (LVC, in the velocity range 540 km s$^{-1}$ < $V$ < 560 km s$^{-1}$, following the nomenclature by Wiklind & Combes 1997) represent gas far from the nucleus (∼1 kpc), there is still no agreement regarding the more redshifted components (HVC, 560 km s$^{-1}$ < $V$ < 640 km s$^{-1}$).

A schematic view of proposed models to describe the almost edge-on disk of CenA is presented in Figure 9. This figure includes edge-on and face-on views of the proposed models within the inner 2 kpc, as well as a qualitative interpretation of the kinematic location of the absorption lines. A warped and thin disk model (e.g., Quillen et al. 2006, 2009; Neumayer et al. 2007) reproduces well the observed emission lines in terms of distribution and kinematics. However, this model is not able to reproduce by itself the existence of the redshifted components (HVC) because it assumes pure circular orbits (Eckart et al. 1999; see Figure 9(a)). It is necessary to augment this model with either diffuse gas (Eckart et al. 1999; see Figure 9(b)) or non-circular/infalling motions (e.g., as suggested in van der Hulst et al. 1983 and Paper I; see Figure 9(c)). Since the implications of the latter two models diverge, we discuss next what is the most plausible one.

It is remarkable that we detect the broad line of the HVC against the brightest continuum source (position *d*) but it is found to be much weaker toward position *c* just ∼0.4 pc next to it and further from the nucleus. This considerably restricts the upper limit of a few hundred parsecs set by VLA data (Sarma et al. 2002). The non-circular/infalling motions within a warped disk model (Figure 9(c)) can provide the observed differences between positions *c* and *d*, since one would expect higher velocities closer to the nucleus. On the other hand, this is not expected in the warped disk with diffuse gas model (Figure 9(b)) since this gas should be distributed at high latitudes up to about a few hundreds of parsecs.

In addition, the physical locations of the different absorbing regions in the line of sight derived from the warped disk with diffuse gas model (Figure 9(b)) are complex. The model predicts that LVC lines 1 and 3 (Figure 7) arise at $r$ = 1.7–1.9 kpc and are separated by up to $\Delta z \simeq 160$ pc from the disk, line 2 should be located $r$ = 200 pc and $\Delta z \simeq 0$, and the HVC lines 4, 5, and 6 at $r$ = 200–600 pc and $\Delta z \simeq 300$ pc (see Figure 9(b)). In this model, within $r$ < 600 pc, the nearer the corresponding absorbing region is to the nucleus the closer the corresponding line velocity is to the systemic velocity.

Finally, no component within the inner $r$ = 200 pc is taken into account in Eckart et al.'s model, although a large concentration of molecular gas is found there (Paper I). A contribution to the molecular gas profile of this component should be seen as an extension of narrow line 2 (arising from $r$ = 200 pc at $\Delta z$ = 0 pc in Eckart et al.'s model). The limit imposed by Eckart et al. (1999) was set at $r$ = 200 pc so that line 2 reproduces the observed one. However, without that constraint, line 2 is difficult to be reproduced in that model.

These arguments suggest that the nature of the HVCs is not just diffuse gas within a warped disk far from the nucleus, and that non-circular motions and/or infalling gas must be important mechanisms to explain the nature of this component. Within this scenario, molecular lines 4, 5, and 6 and atomic lines I/II and III would arise at radii $r \lesssim 1$ kpc, while lines 1, 2, and 3 and SV and IV would be at $r \gtrsim 1$ kpc (Figure 9(c)).

### 6.2. An X-ray Dominated Region (XDR)?

Since a powerful AGN resides in this galaxy, and a significant amount of gas is located within the inner $r$ = 220 pc (Paper I), it is reasonable to think that X-ray radiation plays a major role in modifying the chemical complexity (i.e., dissociating molecular hydrogen into atomic gas, ionizing and heating, etc.).

In fact, the AGN of Centaurus A is characterized by an X-ray luminosity of $L_X \sim 4.8 \times 10^{41}$ erg s$^{-1}$. The incident flux at a

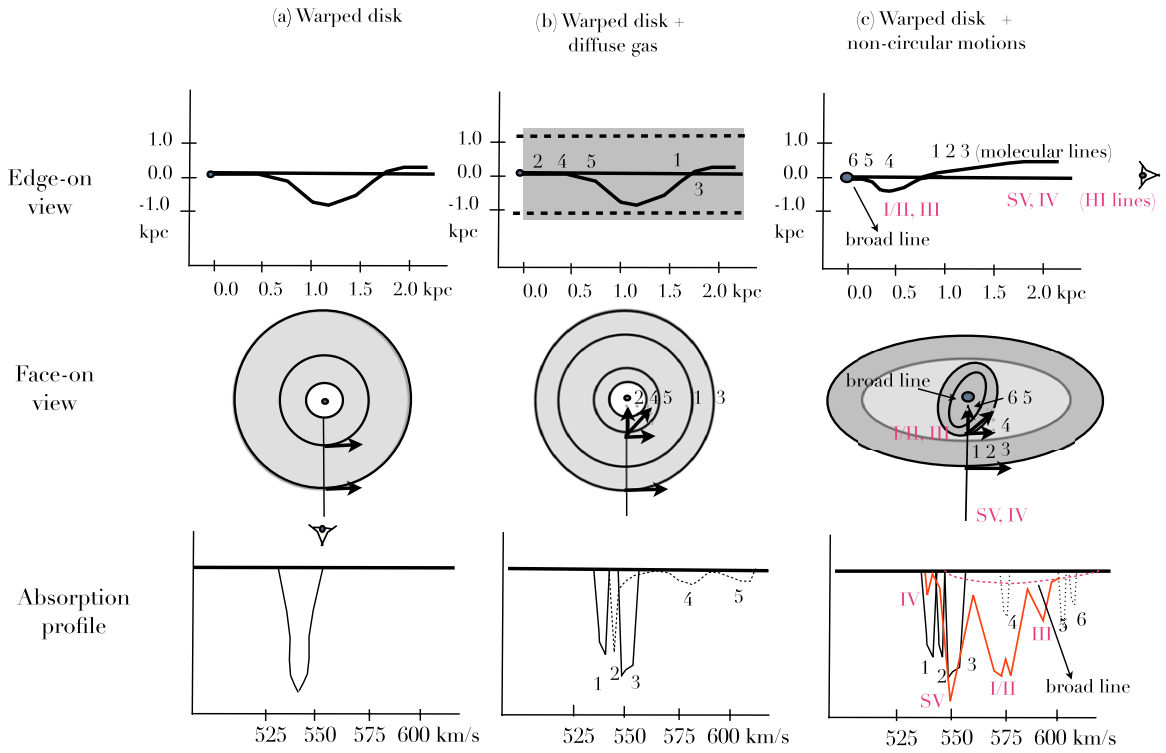


**Figure 9.** Scheme showing the edge-on and face-on views of the proposed models within the inner 2 kpc, as well as the corresponding absorption lines: (a) warped thin disk (as in Quillen et al. 2006), (b) warped disk with diffuse gas (Eckart et al. 1999), and (c) warped disk with a contribution of non-circular motions (weak bar) model (Espada et al. 2009).

(A color version of this figure is available in the online journal.)

distance of 1 pc is thus quite large, $F_X \sim 300$ erg s$^{-1}$ cm$^{-2}$. On the other hand, it is not likely that it has such a strong effect at distances ~100 pc, with fluxes of the order of $F_X \sim 0.03$ erg s$^{-1}$ cm$^{-2}$. The gas column density attenuating these X-rays is estimated to be $\sim 10^{23}$ cm$^{-2}$, probably by a cloud that entirely surrounds the nucleus or by a torus-like structure (Evans et al. 2004 and references therein).

The LVC likely arises from cold molecular gas, with kinetic temperatures $T \sim 10$ K and average hydrogen densities of the order of $n \sim 10^4$ cm$^{-3}$, which seems to be appropriate for the disk as seen in emission (e.g., Eckart et al. 1990b) as well as in absorption (e.g., Wiklind & Combes 1997; Muller & Dinh-V-Trung 2009). Less information is present in the literature for the physical conditions of the HVC, since this weak component is difficult to detect.

Observationally, Wiklind & Combes (1997) show that the average of [HCO$^+$]/[HCN] ~ 1.3 and 1.7, while the average for [HNC]/[HCN] is 0.25 and 0.5, with respect to the LVC and the HVC. The numerical ratios of Meijerink & Spaans (2005) for an X-ray dominated region (XDR) are [HCO$^+$]/[HCN] ~ 1–10 and [HNC]/[HCN] ~ 0.01–1, with $F_X = 160$ erg s$^{-1}$ cm$^{-2}$ and $n_H = 10^{5.5}$ cm$^{-3}$ (or both $F_X$ and $n_H$ 2 orders of magnitude lower). This numerical ratio agrees well with the observations. However, under certain circumstances, a photodissociation region could also reproduce the given molecular gas ratios.

X-rays do not lead to strong dissociation of CO and it can be present in an XDR at elevated temperatures (Spaans 2008). Warm CO gas produces emission originating from high-rotational transitions. Bright CO emission lines have been seen for the first three $J$-levels, and larger $T_{ex}$ (20–30 K) have been inferred for molecular clouds close to the nucleus (e.g., Israel et al. 1991). On the other hand, absorption lines of the lower $J$ transitions will preferentially sample the (excitationally) coldest gas. In the nuclear regions, where higher densities and kinetic temperatures are expected, only high-$J$ transitions of CO would have such broad lines as seen in HCO$^+$(1–0), as it has been suggested with previous CO(3–2) single-dish data (Wiklind & Combes 1997). This is likely the reason why we did not detect the broad line in CO(2–1), but may well be detected in higher transitions of CO. This could be a good test to distinguish the physical condition of the molecular gas closer to the nucleus.

The molecular lines at $V > 605$ km s$^{-1}$, including absorption features 5 and 6, are probably molecular clumps close to or within the H I region from which the H I broad absorption component arises. We consider the possibility that these features are located close to the nucleus (as suggested in Figure 9(c)). For an X-ray illuminated gas like these clouds, the physical conditions of the gas that surrounds the AGN can be studied using the effective ionization parameter, $\xi_{eff}$, which is proportional to the ratio of incident (and attenuated) X-ray photon flux to gas density of the cloud (Maloney et al. 1996). The effective ionization parameter of a molecular cloud can be calculated as

$$\xi_{eff} \sim 1.1 \times 10^{-2} L_{44}/(N_{22}^{0.9} n_9 r^2),$$

where the $L_{44} = L_X/10^{44}$ is the X-ray luminosity of hard photons (energies >2 keV) in erg s$^{-1}$, $n_9$ the gas density of the cloud in $10^9$ cm$^{-3}$, $r$ the distance to the X-ray emitting source in pc, and $N_{22}$ the attenuating gas column density in $10^{22}$ cm$^{-2}$ (Maloney et al. 1994, 1996). The molecular cloud regions are exposed to an X-ray luminosity from Cen A's AGN of $L_X = 4.8 \times 10^{41}$ erg s$^{-1}$ in the hard energy range 2–10 keV (Evans et al. 2004).

If we assume for the molecular gas arising in the two high velocity absorption features 5 and 6 a $T_{ex} = 10$ K, a size of the

1.3 mm continuum of 0.009 pc (Kellermann et al. 1997), and a size of the cloud of $R \simeq 10$ pc then the molecular clouds would be characterized by densities of about $n \sim 10^5$ cm$^{-3}$.

The gas column densities that are attenuating the X-rays are estimated to be $\sim 10^{23}$ cm$^{-2}$ (Evans et al. 2004). By assuming a distance to the nucleus of $r = 10$ pc, it then yields a parameter $\xi_{\rm eff} = 7 \times 10^{-4}$. Then for $r = 1$ pc $\xi_{\rm eff} = 0.1$. A $\xi_{\rm eff} > 10^{-3}$ means that the gas will be predominantly in its atomic phase and it indicates that the molecular clouds must be at $r > 10$ pc in order to survive under the above assumptions. This is in agreement with the smaller [$H_2$]/[H I] ratio found in the HVC with respect to the LVC (Section 5.2).

### 6.3. Physical Properties of the Circumnuclear H I

As mentioned in Section 3.2, the velocity widths of our three main prominent H I features (i.e. I, I/II, and III) are between 5 and 10 km s$^{-1}$. If one neglects line broadening due to rotation and turbulence, and attributes the observed FWHM only to thermal motions in the gas, the line widths shown in Table 2 would indicate temperatures between 800 and 5700 K. Turbulence can account for a line width of about $\sim$5 km s$^{-1}$, at least within our own Galaxy (Burton 1988). Taking this into account, the actual gas temperature is probably between 20 and 2500 K.

The nature of the gas from which the broad absorption lines arise are much less understood. The underlying broader H I absorption line, with a width of $\sim$55 km s$^{-1}$, cannot be attributed solely to thermal motions since it would give too high temperatures ($\sim$60,000 K). As indicated by Sarma et al. (2002) this redshifted broad H I component is probably a blend arising from several complexes rather than a single one. Since it only shows redshifted velocities, it is likely that this component is largely affected by systematic kinematic contributions, such as non-circular and/or infalling motions, and close to the nucleus, mostly within a distance $\lesssim$0.7 pc (0.4 pc from position $c$ to $d$, and 0.3 pc from position $d$ to the actual nucleus; as mentioned in Section 3.1). If the geometry of the absorbing atomic gas is similar to the molecular gas disk/torus in Paper I (inclination $i = 70^\circ$), then the disk-like feature associated with the broad H I line with column densities of about $N$(H I) $\sim 7 \times 10^{20}$ cm$^{-2}$ would have a (non-projected) radius $r \lesssim 2$ pc. However, we cannot rule out other geometries. Also, note that the kinematic coincidence between the broad absorption lines of H I and other molecular lines such as HCO$^+$(1–0) may suggest that the corresponding absorbing molecular regions are physically connected.

The atomic material arising from the broad component likely contributes to fueling the powerful AGN of Centaurus A. Assuming that this H I region is infalling with a velocity of $\sim$37 km s$^{-1}$(mean velocity minus the systemic velocity), a column density of $N$(H I) $\sim 7 \times 10^{20}$ cm$^{-2}$, and a size of 2 pc, we estimate an accretion rate of $2 \times 10^{-3}$ $M_\odot$ yr$^{-1}$, enough to power the required accretion rate of $\sim 1.5 \times 10^{-5}$ $M_\odot$ yr$^{-1}$ obtained from its isotropic radio luminosity (e.g., van Gorkom et al. 1989).

## 7. SUMMARY AND CONCLUSIONS

We present H I and CO(2–1) absorption features toward the nuclear regions of Centaurus A (NGC 5128), using the VLBA and the SMA, respectively.

Our H I observations allow us to discern with sub-parsec resolution the absorption profiles toward the nuclear jet in the inner 5.4 pc. The H I absorption lines are composed of a system of four main narrow lines as well as an underlying broad line (FWHM $\sim$ 55 km s$^{-1}$), in agreement with previous works using lower spatial resolution observations. Interestingly, the underlying broad absorption line in our data is seen to be more prominent toward the central 21 cm continuum component (base of the nuclear jet, although not the nucleus itself) than toward the continuum emission at $\geqslant$0.4 pc from it and further from the nucleus.

We interpret this as a broad velocity component that arises from an absorbing region that is physically close to the AGN itself, and not just as diffuse gas seen in the projection as suggested by Eckart et al. (1999) since the height of such diffuse component is expected to be of the order of a few hundreds of parsec, and thus we would not expect any substantial difference between both positions at a 0.4 pc scale. In addition, the large width of the broad absorption line suggests that the absorbing region is composed of several complexes with systematic non-circular or infalling motions.

As for the molecular gas component, our CO(2–1) interferometric data provide for the first time CO absorption features against the unresolved 1.3 mm continuum emission with minimal contamination by line emission. The narrow lines (likely arising from clouds at large radii from the nucleus) observed in the CO(2–1) and $^{13}$CO(2–1) profile were identified with previously observed molecular lines such as HCO$^+$(1–0) (e.g., Wiklind & Combes 1997; van Langevelde et al. 1995). Overall, our calculated isotopic ratios [$^{12}$C]/[$^{13}$C] $\sim$ 5–17 and the [$^{16}$O]/[$^{18}$O] $\sim$ 70–220 seem to indicate that the molecular clouds producing the observed narrow absorption lines close to the systemic velocity have similar properties to those in the Galactic center. We did not detect any counterpart of the broad absorption line in the CO(2–1) spectrum as that found in H I or other molecular lines, although the noise level in our CO(2–1) profile would have been sufficient to detect this feature if it were as strong as that of HCO$^+$(1–0).

Since both our H I (position $d$) and molecular absorption profiles arise from molecular clouds in front of a similar continuum emission region within $\sim$0.3 pc, we can compare the atomic and molecular gas properties along the line of sight. The abundances of H I to $H_2$ are noticeably different at different velocities. While the LVCs, $V < 560$ km s$^{-1}$, are dominated by molecular gas, the atomic phase gas seems to dominate at 560 km s$^{-1}$ $< V <$ 600 km s$^{-1}$ when the H I line is compared with the molecular gas content as traced by the CO(2–1) line. Although the molecular to atomic gas ratio is not drastically different when we consider the molecular gas traced by HCO$^+$(1–0), there is still a trend for a larger atomic content for components at higher velocities. These distinct signatures suggest that the physical properties, location, and chemistry of the gas producing the broad line are different to those of the components close to the systemic velocity.

Since the gas corresponding to the broad line is likely not far from the AGN, we argue that its properties might be modified by X-rays, which penetrate much farther than UV. The observed abundances of species such as HCO$^+$ and HCN were estimated to be $\sim 10^{-8}$, and abundance ratios [HCO$^+$]/[HCN] $\geqslant$1 and [HNC]/[HCN] $\sim$ 0.5, which seems to agree with the chemistry of an XDR. In the nuclear regions, higher densities and kinetic temperatures are expected. Only high-$J$ transitions would have such broad lines as seen in HCO$^+$(1–0). Since X-rays do not strongly dissociate CO molecules and they can coexist at high temperatures, higher transitions of CO other than CO(2–1) could

trace the broad line component, as has been suggested with previous CO(3–2) single-dish data.

Because of its kinematics, the two narrow redshifted lines at $V > 600$ km s$^{-1}$ found in our CO(2–1) spectrum, as well as in previous $HCO^+$(1–0) spectrum, might be close to the AGN and falling toward it. These molecular clouds are likely at a distance $\gtrsim$10 pc from the AGN so that they can survive the X-ray emission. On the other hand, at distances $\lesssim$10 pc most of the gas will be in its atomic phase, material that is likely contributing to power the AGN of Centaurus A.

We thank the SMA and NRAO staff members who made the observations reported here possible. We also thank A. Sarma for providing the 21 cm continuum VLA data, and S. Martin and I. Jimenez-Serra for interesting discussions. This research has made use of NASA's Astrophysics Data System Bibliographic Services and has also made use of the NASA/IPAC Extragalactic Database (NED) which is operated by the Jet Propulsion Laboratory, California Institute of Technology, under contract with the National Aeronautics and Space Administration. D.E. was supported by a Marie Curie International Fellowship within the 6th European Community Framework Programme (MOIF-CT-2006-40298).

*Facilities:* VLBA, SMA

## REFERENCES

Burton, W. B. 1988, The Structure of our Galaxy Derived from Observations of Neutral Hydrogen, (Galactic and Extragalactic Radio Astronomy; Berlin: Springer-Verlag)
Combes, F. 2008, Ap&SS, 313, 321
Eckart, A., Wild, W., & Ageorges, N. 1999, ApJ, 516, 769
Eckart, A., et al. 1990a, ApJ, 365, 522
Eckart, A., et al. 1990b, ApJ, 363, 451
Espada, D., et al. 2009, ApJ, 695, 116
Evans, D. A., et al. 2004, ApJ, 612, 786
Frerking, M. A., Langer, W. D., & Wilson, R. W. 1982, ApJ, 262, 590
Gardner, F. F., & Whiteoak, J. B. 1976a, Proc. Astron. Soc. Aust., 3, 63
Gardner, F. F., & Whiteoak, J. B. 1976b, MNRAS, 175, 9P
Gupta, N., et al. 2007, ApJ, 654, L111
Harris, G. L. H., Rejkuba, M., & Harris, W. E. 2009, arXiv:0911.3180
Harrison, A., Henkel, C., & Russell, A. 1999, MNRAS, 303, 157
Henkel, C., et al. 1993, A&A, 268, L17
Henkel, C., et al. 2009, A&A, 500, 725
Ho, P. T. P., Moran, J. M., & Lo, K. Y. 2004, ApJ, 616, L1
Horiuchi, S., Meier, D. L., Preston, R. A., & Tingay, S. J. 2006, PASJ, 58, 211
Israel, F. P. 1998, A&AR, 8, 237
Israel, F. P., Raban, D., Booth, R. S., & Rantakyrö, F. T. 2008, A&A, 483, 741
Israel, F. P., van Dishoeck, E. F., Baas, F., de Graauw, T., & Phillips, T. G. 1991, A&A, 245, L13
Israel, F. P., et al. 1990, A&A, 227, 342
Jones, D. L., et al. 1996, ApJ, 466, L63
Kellermann, K. I., Zensus, J. A., & Cohen, M. H. 1997, ApJ, 475, L93
Maloney, P. R., Begelman, M. C., & Rees, M. J. 1994, ApJ, 432, 606
Maloney, P. R., Hollenbach, D. J., & Tielens, A. G. G. M. 1996, ApJ, 466, 561
Meijerink, R., & Spaans, M. 2005, A&A, 436, 397
Meisenheimer, K., et al. 2007, A&A, 471, 453
Muller, S., & Dinh-V-Trung, 2009, ApJ, 696, 176
Muller, S., Guélin, M., Dumke, M., Lucas, R., & Combes, F. 2006, A&A, 458, 417
Neumayer, N., et al. 2007, ApJ, 671, 1329
Prantzos, N., Aubert, O., & Audouze, J. 1996, A&A, 309, 760
Quillen, A. C., Neumayer, N., Oosterloo, T., & Espada, D. 2009, arXiv:0912.0632
Quillen, A. C., Brookes, M. H., Keene, J., Stern, D., Lawrence, C. R., & Werner, M. W. 2006, ApJ, 645, 1092
Roberts, M. S. 1970, ApJ, 161, L9
Sarma, A. P., Troland, T. H., & Rupen, M. P. 2002, ApJ, 564, 696
Schiminovich, D., van Gorkom, J. H., van der Hulst, J. M., & Kasow, S. 1994, ApJ, 423, L101
Seaquist, E. R., & Bell, M. B. 1990, ApJ, 364, 94
Shepherd, M. C., Pearson, T. J., & Taylor, G. B. 1995, BAAS, 27, 903
Solomon, P. M., Sanders, D. B., & Scoville, N. Z. 1979, ApJ, 232, L89
Spaans, M. 2008, in EAS Publications Series 31, Far-Infrared Workshop 2007, ed. C. Kramer, S. Aalto, & R. Simon (Les Ulis: EDP Sciences), 47
Tingay, S. J., & Murphy, D. W. 2001, ApJ, 546, 210
Tingay, S. J., et al. 1998, AJ, 115, 960
van der Hulst, J. M., Golisch, W. F., & Haschick, A. D. 1983, ApJ, 264, L37
van Gorkom, J. H., van der Hulst, J. M., Haschick, A. D., & Tubbs, A. D. 1990, AJ, 99, 1781
van Gorkom, J. H., et al. 1989, AJ, 97, 708
van Langevelde, H. J., Pihlström, Y., & Beasley, A. 2005, Ap&SS, 295, 249
van Langevelde, H. J., van Dishoeck, E. F., Sevenster, M. N., & Israel, F. P. 1995, ApJ, 448, L123
Wang, M., et al. 2004, A&A, 422, 883
Wiklind, T., & Combes, F. 1997, A&A, 324, 51
Wild, W., Eckart, A., & Wiklind, T. 1997, A&A, 322, 419
Wilson, T. L., & Rood, R. 1994, ARA&A, 32, 191